Journal of the Mechanics and Physics of Solids 132 (2019) 103676

Contents lists available at ScienceDirect

Journal of the Mechanics and Physics of Solids

journal homepage: www.elsevier.com/locate/jmps

Plastic contact of self-affine surfaces: Persson's theory versus discrete dislocation plasticity

S.P. Venugopalan [a], N. Irani [a], L. Nicola [a,b,*]

[a] Department of Material Science and Engineering, Delft University of Technology, the Netherlands
[b] Department of Industrial Engineering, University of Padova, I-35131 Padua, Italy

ARTICLE INFO

Article history:
Received 10 February 2019
Revised 19 July 2019
Accepted 28 July 2019
Available online 29 July 2019

Keywords:
Persson's theory
Contact mechanics
Self-affine surfaces
Plasticity
Dislocation dynamics

ABSTRACT

Persson's theory allows for a fast and effective estimate of contact area and contact stress distributions when a flat and a self-affine rough surface are pressed into contact. For elastic bodies, the results of the theory have been shown to be in very good agreement with rather costly simulations. The theory has also been extended to plastic bodies. In this work, the results of Persson's theory for plastic bodies are compared with those of discrete dislocation plasticity. The area–load curves obtained by theory and simulations are found to be in good agreement when the rough surface has a very small root-mean-square (rms) height. For larger rms heights, which are more realistic for metal surfaces, the agreement is no longer good unless in the theory, instead of a size-independent material strength, one uses a rms height- and resolution-dependent yield strength. A modification of this type, i.e., the use of a yield strength dependent on size, does however not lead to agreement between the probability distributions of the contact stress, which is much broader in the simulations than in the theory. The most likely reason for this discrepancy is that the theory, apart from neglecting plasticity size dependence, only applies to elastic-perfectly plastic bodies and therefore, neglects strain hardening.

1. Introduction

In the past decades, numerous experiments have confirmed that surfaces have a self-affine fractal character down to the nanoscale (Bouchaud, 1997; Bouchaud et al., 1990; Dauskardt et al., 1990; Imre et al., 1992; Krim and Palasantzas, 1995; Lechenault et al., 2010; Majumdar and Tien, 1990; Mandelbrot et al., 1984; Plouraboué and Boehm, 1999). To account for this, Persson (2001b) developed a contact model that includes the presence of roughness on successive length scales. At a given nominal pressure, his theory can predict the contact area, contact stress distribution and interfacial separation of elastic bodies in good agreement with experiments (Lorenz and Persson, 2009a; 2009b; Persson, 2001b). Persson's theory has also been extended to study plasticity (Persson, 2001a). However, to the best of the authors knowledge, the validity of Persson's theory has never been tested for metal surfaces that deform plastically. Here, we intend to test the theory by comparing its results with those of two-dimensional discrete dislocation plasticity simulations.

* Corresponding author at: Department of Material Science and Engineering, Delft University of Technology, the Netherlands.
E-mail addresses: syam.venugopal@gmail.com (S.P. Venugopalan), nil.irani@gmail.com (N. Irani), l.nicola@tudelft.nl (L. Nicola).

https://doi.org/10.1016/j.jmps.2019.07.019

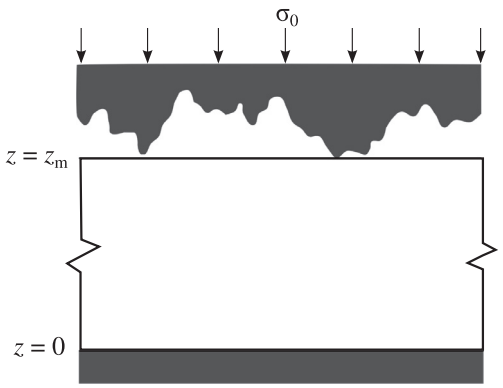

Fig. 1. Schematic representation of the metal slab indented by a rough surface.

Metallic rough surfaces span various orders of length scales, with asperities as small as a few nanometers. Already at the micro-scale, experiments have shown that plasticity is size dependent (Fleck et al., 1994; Greer et al., 2005; Ma and Clarke, 1995; Volkert and Lilleodden, 2006). The size dependence entails that, differently from the elastic response, the plastic response does not scale with size. Although the size effect cannot be captured by classical plasticity, which does not contain any material length scale, it is captured by non-local plasticity theories (Nix and Gao, 1998; Gurtin, 2000) and by numerical simulations of the type of discrete dislocation plasticity (DDP) (El-Awady, 2015; Kraft et al., 2010; Nicola et al., 2003). The latter contains various length scales, including the dislocation Burgers vector, and the average spacing between dislocation sources and dislocation obstacles. Recently, Venugopalan and Nicola (2019) performed dislocation dynamics simulations to study indentation of metal crystals by self-affine rigid indenters with various roughness parameters. Results showed indeed a size dependence when scaling the dimensions of the rough body: the pressure-displacement response does not scale and smaller bodies are stronger. This phenomenon is mostly caused by limited dislocation availability, i.e., when the stressed subsurface regions become too small, they no longer contain a sufficient amount of dislocation sources to sustain plastic deformation. The same phenomenon is observed in Venugopalan and Nicola (2019) when indenting a crystal with constant size and a surface with smaller root mean square roughness: if pressure is normalized on the root mean square slope and interference is normalized by the rms height, the results are elastically identical, but not plastically. The crystal indented by the largest rms-height is subjected to a broader stressed region underneath the surface and is more susceptible to plastic deformation and, therefore, is softer. The characteristic scale-independent material length scale is the average spacing between dislocation sources.

In order to include size-dependent plasticity in his theory, Persson suggested to replace the constant material yield strength with a resolution-dependent yield strength, i.e., a yield strength that increases with decreasing the short wavelength cut-off λ_s (Persson, 2006). The exact dependence of yield strength on resolution was not specified and it might be inferred by comparison with dislocation dynamics simulations, if the results are otherwise in agreement.

Before proceeding with the comparison it is important to note that the GFDD simulations are based on the small strain and small slope approximation. This means that for rms heights realistic for metals one can only reach partial closure of the contact. Persson's original theory is instead exact at full contact and requires a correcting factor at partial contact (Dapp et al., 2014; Manners and Greenwood, 2006; Wang and Müser, 2017). Therefore, for the sake of comparison, we will start by showing the results of GFDD simulations for a very small rms height, which is not observed in typical metal surfaces but allows to reach closure. This is the case for which the best agreement is found between simulation and theory. We will then see that for surfaces with rms heights more typical for metals, the agreement is not good.

2. Formulation of the problem

A rigid indenter with self-affine roughness is pressed into contact against a metallic slab of finite height, see Fig. 1. The power spectrum of the indenter is

$$\begin{aligned} C(q) &= C_0 \left(\frac{q}{q_0}\right)^{-2(H+\frac{1}{2})} && \text{if } q_0 < q < q_s, \\ C(q) &= 0 && \text{else}, \end{aligned} \tag{1}$$

where $q_0 = 2\pi/\lambda_l$ and $q_s = 2\pi/\lambda_s$ are the wavenumbers corresponding to the long and short wavelengths cut-offs, i.e. λ_l and λ_s, respectively. C_0 is determined by the root-mean-square (rms) height $\bar{h}$ as

$$\bar{h}^2 = 2\int_{q_0}^{q_s} C(q)\, dq. \tag{2}$$

Assuming $q_s >> q_0$ implies that

$$C_0 = \frac{H\bar{h}^2}{q_0}, \tag{3}$$

where H is the Hurst exponent. The power-law scaling for the surface height spectrum applies to wavenumbers between cut-offs at long and short wave numbers $q_0 < q < q_s$.

The slab is taken to be elastically isotropic with Young's modulus $E = 70$ GPa and Poisson's ratio $\nu = 0.33$, representative values for aluminum. Moreover, it has a finite height z_m. The top surface of the crystal is frictionless at the points of contact, $\sigma_{xz}(x^c, z_m^c) = 0$, and traction-free elsewhere, $\sigma_{xz}(x^{nc}, z_m^{nc}) = \sigma_{zz}(x^{nc}, z_m^{nc}) = 0$ The superscripts 'c' and 'nc' stand for points 'in contact' and points 'not in contact', respectively. Furthermore, the bottom of the substrate is kept fixed: $u_x(x, 0) = u_z(x, 0) = 0$.

2.1. Persson's theory for line contacts in solids with finite height

Under the assumption that at resolution q the contact is full, Persson (2001a,b) states that on all length scales the distribution of contact stress σ is

$$P(\sigma, q) = \langle \delta(\sigma - \sigma_{\text{nom}}) \rangle. \tag{4}$$

Here, σ_{nom} is the nominal contact stress when the surface roughness with wavenumbers larger than q have been smoothed out and $\langle \ldots \rangle$ stands for ensemble averaging over different surface roughness profiles. As finer roughness features are added, the contact stress distribution becomes $P(\sigma, q + \Delta q) = \langle \delta(\sigma - (\sigma_{\text{nom}} + \Delta\sigma)) \rangle$. By expanding this equation to linear order in Δq

$$\frac{\partial P}{\partial q} = k(q)\ \frac{\partial^2 P}{\partial \sigma^2}, \tag{5}$$

where

$$k(q) = \frac{\langle \Delta\sigma^2 \rangle}{2\,\Delta q}. \tag{6}$$

The partial differential Eq. (5) can be solved by imposing the following boundary conditions:

$$P(0, q) = 0, \tag{7a}$$

$$P(\sigma, 0) = \delta(\sigma - \sigma_0), \tag{7b}$$

$$P(\sigma_Y, q) = 0. \tag{7c}$$

The boundary conditions enforce that: (7a) when the local contact stress reaches zero, contacting surfaces detach; (7b) at the lowest resolution, the stress distribution is a delta function; (7c) the contact stress does not exceed the yield strength σ_Y. The latter condition entails that Persson's theory for plasticity applies to ideal elasto-plastic solids that display no work hardening. Notice also that solving an elastic contact problem is equivalent to imposing $\sigma_Y \to \infty$ in Eq. (7c).

Following Persson (2001a,b), the solution to Eq. (5) with boundary conditions (7a)–(7c) can be written as

$$P(\sigma, q) = \sum_{n=1}^{\infty} A_n(q)\ \sin\left(\frac{n\pi\sigma}{\sigma_Y}\right). \tag{8}$$

Substituting the expression above in Eq. (5) leads to the following partial differential equation:

$$\frac{\mathrm{d}A_n}{\mathrm{d}q} = -k(q)\left(\frac{n\pi}{\sigma_Y}\right)^2 A_n, \tag{9}$$

which after solution leads to

$$A_n(q) = \frac{2}{\sigma_Y}\ \sin(\alpha_n)\ \exp\left[-\left(\frac{n\pi}{\sigma_Y}\right)^2 \int_{q_0}^{q} k(q')\,\mathrm{d}q'\right]. \tag{10}$$

The full expression of the contact stress distribution is then given by

$$P(\sigma, q) = \frac{2}{\sigma_Y} \sum_{n=1}^{\infty} \sin(\alpha_n)\ \exp\left[-\alpha_n^2 L(q)\right] \sin\left(\frac{n\pi\sigma}{\sigma_Y}\right), \tag{11}$$

where $\alpha_n = \dfrac{n\pi\sigma_0}{\sigma_Y}$ and $L(q) = \int_{q_0}^{q} \dfrac{k(q')}{\sigma_0^2}\,\mathrm{d}q'$. In order to solve Eq. (5), one must obtain $k(q)$ from $\Delta\sigma(q)$. Wang and Müser (2017) showed that for elastic substrates with a finite height, $\Delta\sigma$ is given by

$$\Delta\sigma(q) = \sqrt{W(a_r)}\left(\frac{qE^* f(q)}{2}\right) \mid \tilde{h}(q) \mid, \tag{12}$$

where a_r is the relative contact area, and E^* is the effective elastic modulus. Moreover, $W(a_r)$ is the correction introduced by Wang and Müser (2017) for the low load regimes, i.e., when contact is partial. Furthermore, for frictionless elastic contacts, a substrate of height z_m, and a fixed bottom, $f(q)$ is given by Venugopalan et al. (2017b) as

$$f(q) = \frac{\cosh(2qz_m) + 2(qz_m)^2 + 1}{\sinh(2qz_m) - 2qz_m}, \tag{13}$$

and

$$k(q) = \frac{\langle \Delta\sigma^2 \rangle}{2\Delta q} = \frac{1}{2} W[a_r(q)] \left(\frac{qE^* f(q)}{2} \right)^2 | \tilde{h}(q) |^2 . \tag{14}$$

Finally, for the power spectrum $C(q)$ in this work

$$k(q) = \frac{H\bar{h}^2 q_0}{8} W(a_r) (E^* f(q))^2 \left(\frac{q}{q_0} \right)^{1-2H}. \tag{15}$$

Having found $k(q)$, we may then proceed to solve the partial differential Eq. (5).

Subsequently, from the contact stress distribution P(σ, q), following Persson (2001a,b), one can obtain the following quantities:

(i) The fraction of macro-contact area that is not in real contact a_r^{non}, that forms a plastic contact a_r^{plas}, and an elastic contact a_r^{elas}:

$$\begin{aligned} a_r^{non} &= \int_{q_0}^{q} k(q') \frac{\partial P}{\partial \sigma}(0, q') \, dq' \\ &= \frac{2}{\pi} \sum_{n=1}^{\infty} \frac{\sin(\alpha_n)}{n} \left(1 - \exp\left[-\alpha_n^2 L(q)\right]\right), \\ a_r^{plas} &= -\int_{q_0}^{q} k(q') \frac{\partial P}{\partial \sigma}(\sigma_Y, q') \, dq' \\ &= -\frac{2}{\pi} \sum_{n=1}^{\infty} (-1)^n \frac{\sin(\alpha_n)}{n} \left(1 - \exp\left[-\alpha_n^2 L(q)\right]\right), \\ a_r^{elas} &= 1 - a_r^{plas} - a_r^{non}. \end{aligned} \tag{16}$$

(ii) The relative contact area a_r, comprising both the area in elastic and plastic contact:

$$a_r = 1 - a_r^{non}. \tag{17}$$

2.2. Green's function dislocation dynamics

At each time step of the simulation, the solution of the boundary value problem in Fig. 1 is obtained by the superposition of two linear elastic solutions: The elastic analytical fields for dislocations in a homogeneous infinite solid, and the solution to the complementary elastic boundary-value problem, which corrects for the boundary conditions. The methodology is similar to Van der Giessen and Needleman (1995), however, the solution to the complementary elastic boundary-value problem is obtained through Green's function molecular dynamics (GFMD) (Venugopalan et al., 2017a).

The schematics of the indented single crystal is shown in Fig. 2. Indentation is performed by applying the displacement U_z on top of the rigid indenter from which the value of the equivalent applied pressure σ_0 is obtained.

Following Van der Giessen and Needleman (1995), the dislocation dynamics are controlled by constitutive rules inspired by atomic scale phenomena that control the nucleation and glide of the dislocations. The crystal is initially dislocation free, and contains a given density of slip planes, dislocation sources, and obstacles that are randomly distributed. When the stress in the body reaches the nucleation strength $\bar{\tau}_{nuc}$ on a dislocation source for a given amount of time t_{nuc}, a dislocation dipole is nucleated from the sources and glides on the slip plane resulting in plastic deformation. The velocity with which the dislocations glide is controlled by the Peach-Koehler force acting on them. Dislocations are stopped by the obstacles, but released when the resolved shear stress on them exceeds the critical strength associated to the obstacle, τ_{obs}.

2.2.1. Choice of parameters for the simulations

Dislocations are nucleated from randomly distributed nucleation sources on slip planes oriented at $\phi = 60^\circ$, -60°, and 90° with respect to the loading direction. The simulations are performed for a nucleation source density $\rho_{nuc} = 40\ \mu m^{-2}$. In both cases, the sources have a Gaussian strength distribution with the mean strength being $\bar{\tau}_{nuc} = 50$ MPa. The nucleation time $t_{nuc} = 10$ ns. The density of obstacles is $\rho_{obs} = 40\ \mu m^{-2}$ and the obstacle strength is $\tau_{obs} = 150$ MPa. The drag coefficient for glide is $B = 10^{-4}$ Pa s and the critical distance for annihilation is $L_e = 6b$, where $b = 2.5 \times 10^{-4}$ μm is the magnitude of the Burgers vector. Moreover, in all calculations a time step of $\Delta t = 2.5$ ns is employed. The GFDD simulations are performed for 10 realizations of nucleation source and obstacle distributions. In the following, the presented results are obtained by averaging over these 10 realizations.

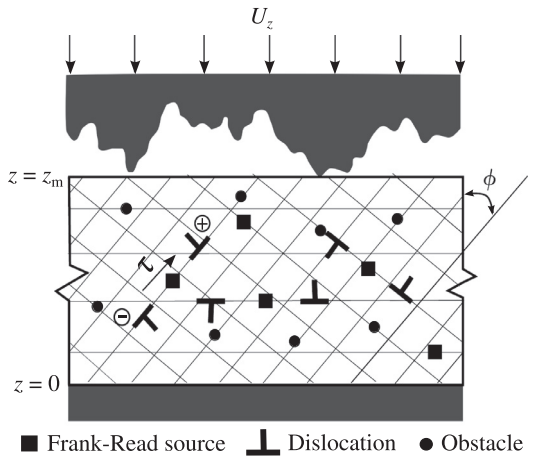

Fig. 2. Schematic representation of the metal crystal indented by a rough surface.

Table 1
Default simulation parameters.

Parameters	Notation	Value
Angle between slip planes and loading direction	ϕ	$60^\circ, -60^\circ, 90^\circ$
Source density	ρ_{nuc}	$40\ \mu\text{m}^{-2}$
Mean nucleation strength	$\bar{\tau}_{\text{nuc}}$	50 MPa
Obstacle density	ρ_{obs}	$40\ \mu\text{m}^{-2}$
Obstacle strength	τ_{obs}	150 MPa
Drag coefficient	B	10^{-4} Pas
Length of the Burger's vector	b	$2.5 \times 10^{-4}\ \mu$m
Critical annihilation length	L_e	$6b$
Time step	Δt	2.5 ns
Thermodynamic discretization	ϵ_{t}	2^{-1}
Fractal discretization	ϵ_{f}	$16^{-1}, 32^{-1}, 64^{-1}$
Continuum discretization	ϵ_{c}	32^{-1}
Hurst exponent	H	0.8
Long wavelength cut-off	λ_{l}	10 μm
Rms height	$\bar{h}$	0.001, 0.01, 0.1 μm
Height of the crystal	z_{m}	10 μm

The roughness of the indenter is obtained using the power spectral density method (Campañá et al., 2008). The power spectrum $C(q)$ is used to construct a periodic self-affine surface with a Gaussian height distribution. The Fourier transform of the height profile $h(r)$ of the indenter is given as:

$$\tilde{h}(q) = h_0\ \tilde{\Delta}_{\text{G}}(q)\sqrt{C(q)} = h_0\ \frac{\tilde{\Delta}_{\text{G}}(q)}{q^{\left(\frac{1}{2}+H\right)}}, \tag{18}$$

where h_0 is a real-valued constant which can be adjusted to obtain the required rms slope of the surface, $\tilde{\Delta}_{\text{G}}(q)$ is a Gaussian random variable with random phase such that $\langle\tilde{\Delta}_{\text{G}}(q)\rangle = 0$, and H is the Hurst exponent. For different realizations of the rough surface, all parameters, including the cut-off values, are kept fixed except the Gaussian random variable $\tilde{\Delta}_{\text{G}}(q)$ whose phase is randomly varied. Furthermore, before starting the simulations the surfaces so generated are shifted such that the lowest point touches the substrate at zero interfacial pressure. The fractal discretization, $\epsilon_{\text{f}} = \lambda_{\text{s}}/\lambda_{\text{l}}$, defines the range of wavelengths used to describe the surface. Here, the long wavelength cut-off is kept constant, i.e. $\lambda_{\text{l}} = 10\ \mu$m and the short wavelength cut-off is varied while ϵ_{f} is varied. The thermodynamic discretization is defined as $\epsilon_{\text{t}} = \lambda_{\text{l}}/L_x = 1/2$, where L_x is the width of the periodic unit cell. In the limiting case of $\epsilon_{\text{t}} \to 0$, which corresponds to the thermodynamic limit, the surface is no longer periodic since $L_x \to \infty$. Finally, the continuum discretization is defined as $\epsilon_{\text{c}} = a_0/\lambda_{\text{s}} = 1/32$ where a_0 is the spacing between the grid points that discretize the surface of the substrate. In the limiting case of $\epsilon_{\text{c}} \to 0$, the grid spacing $a_0 \to 0$ and hence the surface has a continuum representation, therefore the solution must converge to the continuum mechanics solution. We selected for the Hurst exponent the value $H = 0.8$, since it is typical for many metallic surfaces (Bouchaud et al., 1990; Dauskardt et al., 1990). The long wavelength cut-off λ_{l} is kept constant and equal to 10 μm. The short wavelength cut-off is changed in the simulations to represent a change in the resolution in Persson's theory. The rms height values considered are $\bar{h} = 0.001,\ 0.01,$ and $0.1\ \mu$m, the latter being the most realistic for metal surfaces.

The simulation parameters are summarized in Table 1.

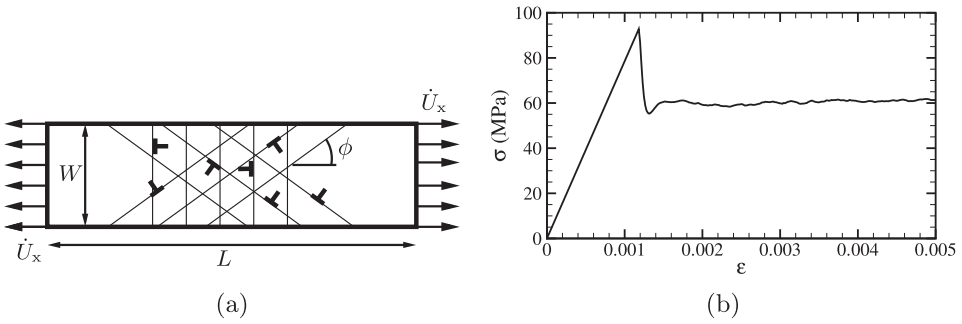

Fig. 3. (a) Schematics of the uniaxial tensile test. (b) Uniaxial tensile stress–strain ($\sigma - \varepsilon$) curve from discrete dislocation plasticity.

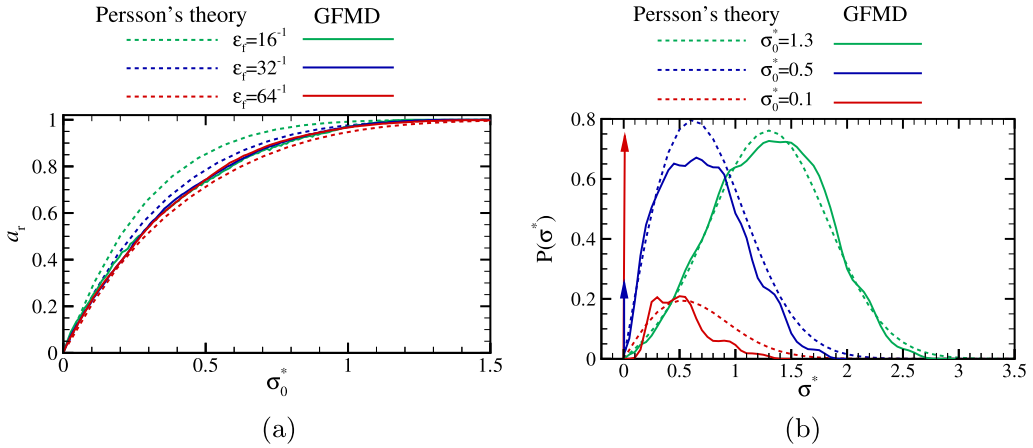

Fig. 4. (a) Relative contact area a_r against reduced applied pressure σ_0^* for indenters with $\bar{h} = 0.001$ μm and three fractal discretizations ϵ_f. (b) Probability distribution of reduced contact stress σ^* for an indenter with $\epsilon_f = 16^{-1}$ at three instances of applied pressure $\sigma_0^* = 0.1$, 0.5 and 1.3.

2.3. The yield strength

While in Persson's theory the yield stress is an input to the calculation, in discrete dislocation plasticity it is an output. To calculate it, we perform a uniaxial tensile loading simulation on a single crystal with the material properties mentioned above.

The dimensions of the crystal are selected to be large enough to not experience size effects and are $L = 12.5$ μm and $W = 5$ μm. The schematics of the uniaxial tensile test is shown in Fig. 3(a). The predicted nominal tensile stress versus applied strain $\varepsilon = 2U_x/L$ is presented in Fig. 3(b). This figure shows that the tensile yield strength of the crystal is $\sigma_Y^{\text{Tensile}} =$ 60 MPa. It is important to highlight that the yield strength identified with $\sigma_Y^{\text{Tensile}}$, here and throughout the manuscript is a size-independent quantity.

3. Persson's theory: correcting factor at low loads for various fractal discretizations

The expression for the elastic energy in Persson's theory was corrected by Wang and Müser (2017) in order to hold at low loads. The correcting factor in the fractal limit, $\lambda_s \to 0$, was given by the authors as

$$W[a_r(\sigma_0^*)] = 1 + c_1(1 - a_r(\sigma_0^*)^2) + c_2(1 - a_r(\sigma_0^*)^4), \tag{19}$$

where $\sigma_0^* = \dfrac{\sigma_0}{E^*\bar{g}}$ is the reduced pressure, σ_0 is the applied pressure and $\bar{g}$ is the root-mean-square gradient of the indenter. Selecting the values of 2/9 and −2/3 for the constants c_1 and c_2 leads to good correspondence between Persson's theory and elastic GFMD simulations.

In this work, we intend to consider fractal discretizations also far from the limit, namely $\epsilon_f = 64^{-1}, 32^{-1}$, or 16^{-1}. To this end, we first proceed to check to which extent the correction factor is independent of fractal discretization. This is done by comparing in Fig. 4(a) the results of Persson's theory with our elastic GFMD calculations for an indenter with rms height $\bar{h} = 0.001$ μm.

Table 2
Coefficients c_1 and c_2 in Eq. (19).

	$\epsilon_f = 16^{-1}$	$\epsilon_f = 32^{-1}$	$\epsilon_f = 64^{-1}$
c_1	−2.3	−0.6	0.19
c_2	1.9	0.2	−0.6

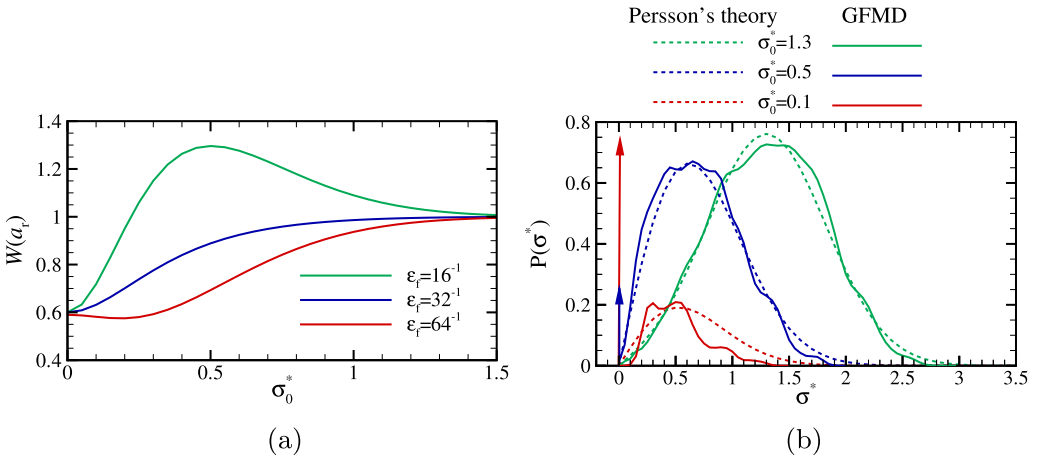

Fig. 5. (a) The correction factor $W(a_r)$ for three different fractal discretizations ϵ_f. (b) Probability distribution of the reduced contact stress σ^* for an indenter with $\epsilon_f = 16^{-1}$ at three instances of applied pressure $\sigma_0^* = 0.1,\ 0.5$ and 1.3.

The results of the relative contact area versus applied load in Fig. 4(a) show that there is a small discrepancy between GFMD and Persson's theory at intermediate load. This corresponds to a non-negligible difference in the probability distribution of the contact stress $P(\sigma^*)$ for larger fractal discretizations, as shown in Fig. 4(b).

To assure that at least our elastic simulations agree well with Persson's theory, we proceed to search for the c_1 and c_2 coefficients that minimize the difference between the area–load curves for theory and simulations. The values, which are non-unique, are listed in Table 2 and lead to the correction factors in Fig. 5(a) and to the contact stress distributions in Fig. 5(b).

We have verified that the correction factors $W(a_r)$ found for indenters with rms height $\bar{h} = 0.001$ μm are also appropriate for the other rms heights used in this work, and are therefore used throughout the manuscript.

4. Comparison between theory and simulations for indenters with small rms height

We start by comparing Persson's theory with GFDD simulations for the indentation of a metal crystal by a rigid indenter with surface roughness with $\bar{h} = 0.001$ μm and fractal discretization $\epsilon_f^{-1} = 64$. This allows to reach near full closure with dislocation dynamics simulations while still obeying the small strain and small slope approximations.

In Persson's plasticity theory, the yield strength σ_Y is an input parameter, which has been interpreted as either the tensile yield strength of the material $\sigma_Y^{\text{Tensile}}$ or the macroscopic indentation hardness, estimated by Johnson (1987) to be $3\,\sigma_Y^{\text{Tensile}}$. By comparison between theory and simulations we assess which of the two definitions is most appropriate: Fig. 6(a), shows a much better agreement between the area–load curves when hardness is used for the definition of σ_Y.

Fig. 6 (b) shows, the relative contact area together with how the elastic a_r^{elas} and plastic a_r^{plas} fractions of contact change with load. Remember that a_r^{elas} and a_r^{plas} are calculated separately in Persson's theory (see Eq. (16)). Thus, it is possible to see that the portion of contact undergoing elastic deformations, a_r^{elas}, initially increases with load, σ_0^*, and then decreases with increasing plasticity. Instead, the relative plastic contact area, i.e. a_r^{plas}, continues to increase with load until the external load reaches $\sigma_0^* = 1.3$. This load corresponds to the point at which the contact stress is everywhere plastic and equal to σ_Y. Notice that the contact in dislocation dynamics simulations never reach full closure, as can be seen from the decrease of the interfacial gap in Fig. 7(a) and a snapshot of the interface at $\sigma_0^* = 1.3$ in Fig. 7(b). The depth of the valleys formed during deformation can be as large as the rms height $\bar{h}$ of the indenter. This is in agreement with the observation of Bowden and Tabor (2001) according to whom full closure is impossible for rough metal surfaces due to work hardening.

Fig. 8 presents the distribution of contact stress for three instances of the applied pressure, $\sigma_0^* = 0.1,\ 0.5$, and 1.3. The probability distribution function representing the plastic part of the contact is a delta peak at $\sigma^* = \sigma_Y^*$. The other delta peak at $\sigma^* = 0$ represents the part of the surface which is not in contact. The area under the probability distribution curve in Persson's theory is the elastic fraction of the contact area a_r^{elas}. This is different from the distribution function obtained through GFDD simulations, where the area under the curve represents the relative contact area a_r: elastic and plastic contact

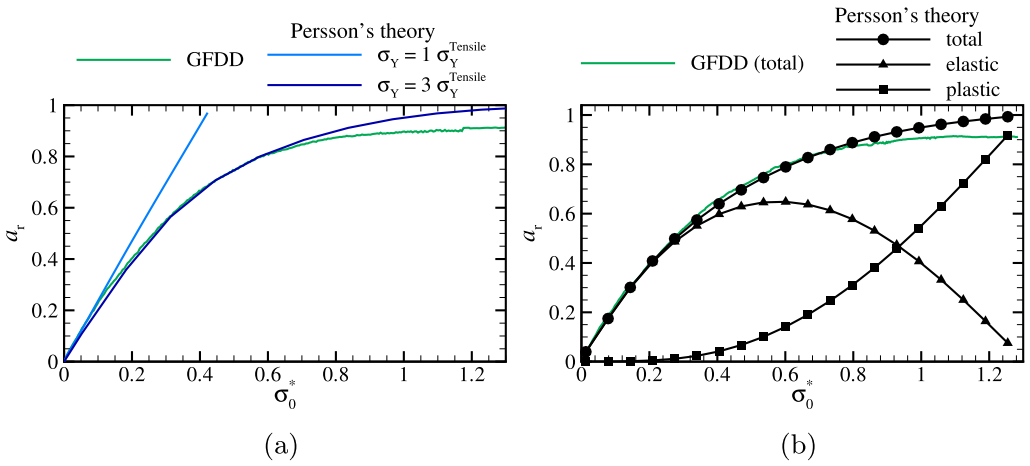

Fig. 6. Relative contact area a_r calculated using GFDD and modified-Persson's theory. In the latter, yield strength $\sigma_Y = \sigma_Y^{\text{Tensile}}$ and $3\,\sigma_Y^{\text{Tensile}}$ were applied as an input.

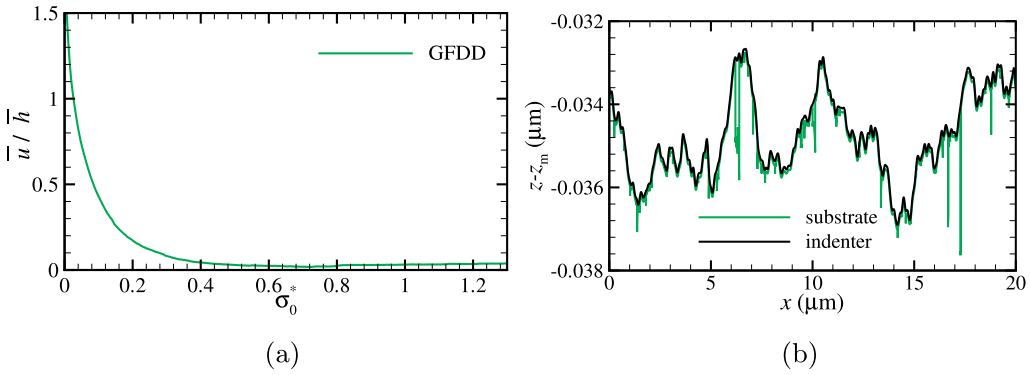

Fig. 7. (a) The average interfacial separation $\bar{u}/\bar{h}$ are plotted against reduced applied pressure σ_0^* for the case of an indenter with $\bar{h} = 0.001$ μm and $\epsilon_f^{-1} = 64$. The input yield strength to Persson's theory is $\sigma_Y = 3\,\sigma_Y^{\text{Tensile}}$. (b) The snapshot of the contact between the indenter and the substrate at $\sigma_0^* = 1.3$.

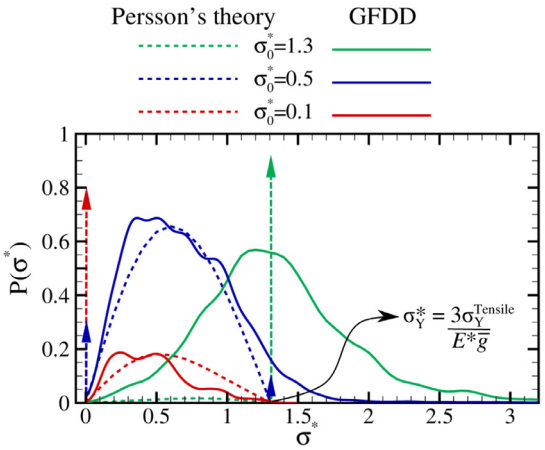

Fig. 8. Probability distribution of the contact stress σ^* at three instances of loading, $\sigma_0^* = 0.1$, 0.5, and 1.3, for an indenter with $\bar{h} = 0.001$ μm and $\epsilon_f^{-1} = 64$.

areas are not distinguished, nor distinguishable, and the deformation only 'partially plastic'. Therefore, agreement between the contact stress distribution obtained by Persson's theory and by the GFDD simulations ceases to be good when plasticity becomes relevant. The simulations predict a much broader stress distribution, with contact stresses larger and smaller than the macroscopic hardness. The reason for this discrepancy can be partly attributed to the fact that Persson's plasticity theory does not account for material hardening. In our opinion, a better agreement with the simulations would be found, if the

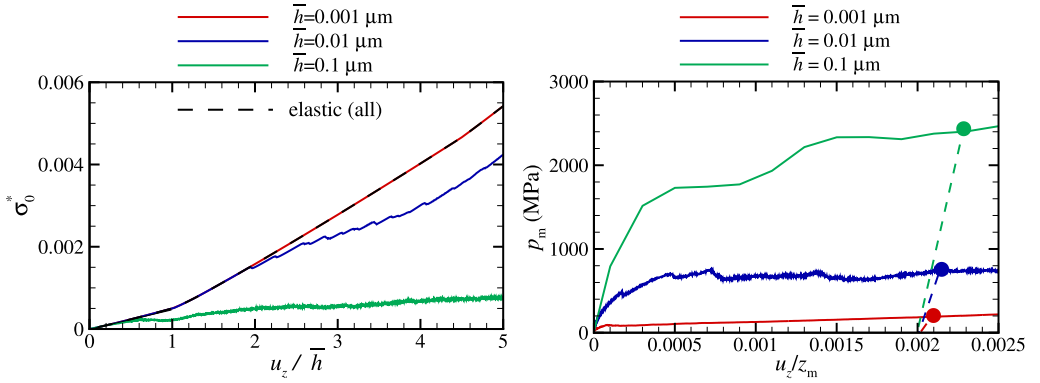

Fig. 9. (a) Reduced nominal pressure and (b) mean contact pressure are plotted against reduced displacement for three different rms heights.

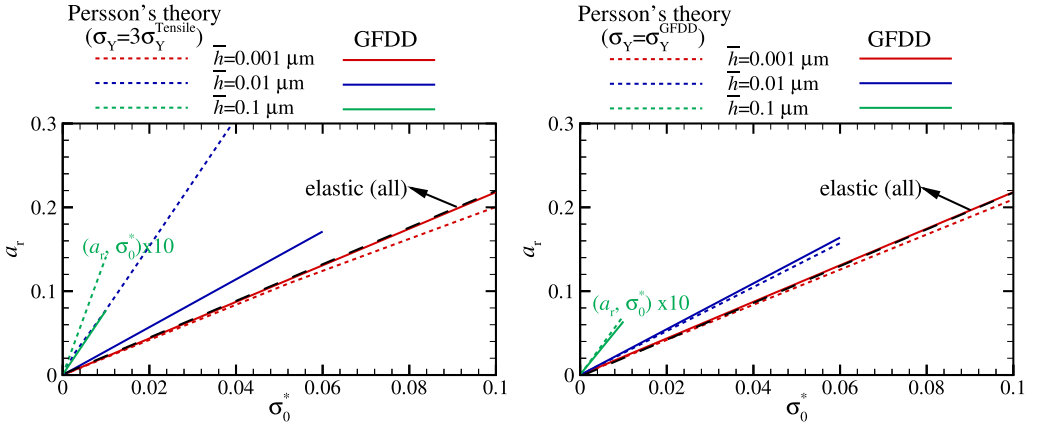

Fig. 10. (a) Relative contact area a_r against reduced applied pressure σ_0^* for an indenter with $\epsilon_f = 64^{-1}$ and three rms heights $\bar{h}$. The input yield strength to Persson's theory is 3 $\sigma_Y^{Tensile}$. (b) The input yield strength to Persson's theory is the indentation yield strength obtained through GFDD calculations.

theory would be slightly modified by making σ_Y^* increase with plastic deformation. The plastic peak will then shift to the right during indentation and the elastic contribution would become more pronounced than it is now.

4.1. Size dependence

It was shown by Venugopalan and Nicola (2019) that when indenting a metal crystal, indenters with different rms heights give rise to the same reduced pressure for equal reduced interference values. However, they induce a different plastic response. The smaller the rms height the later the onset of plastic deformation. This plasticity size dependence occurs because the size of the subsurface region where the dislocation nucleation strength is exceeded scales with rms height, but the availability of dislocation sources does not scale accordingly: the spacing between dislocation sources is a material parameter which is scale independent. This is why a larger reduced pressure is required to induce nucleation in the case of a small rms height.

Fig. 9 presents curves of reduced pressure versus reduced interference, obtained through GFMD simulations, for three indenters of rms heights $\overline{h} = 0.001, 0.01$ and 0.1 μm, together with the corresponding curves of mean contact pressure as a function of displacement. Here, the mean contact pressure is calculated as $p_m \equiv F/A$, where F is the total interfacial force and A is the true contact area. Notice that in Fig. 9 the difference between the curves is solely caused by plasticity.

The relative contact area a_r, as calculated by GFDD and modified Persson's theory, are shown in Fig. 10 for indenters with $\epsilon_f = 64^{-1}$ and various rms-heights. For all indenters, the input yield strength to Persson's theory is assumed to be 3 $\sigma_Y^{Tensile}$. It can be seen that under this assumption, the contact area as predicted by the theory and GFDD are very different from each other when $\bar{h} = 0.01$ μm.

It is noteworthy that scaling rms height corresponds to a vertical shift in the power spectrum of the roughness, and has no influence on the range of wavelengths considered in the problem: both large and small wavelength are the same as before. Already this observation is sufficient to conclude that considering a resolution-dependent yield strength in Persson's theory, i.e. $\sigma(\lambda_s)$, would not improve the agreement between simulations and theory in this case. Instead, it is possible to see in Fig. 10b that if the size-dependent yield strength obtained through dislocation dynamics simulations σ_Y^{GFDD} is used

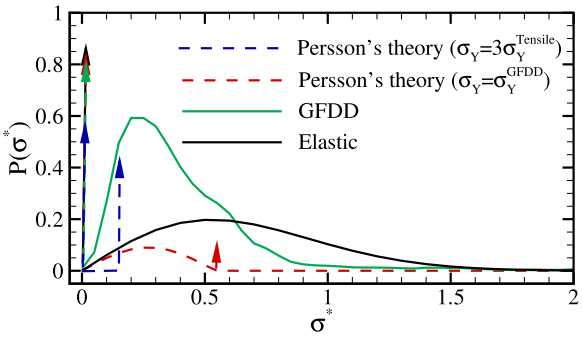

Fig. 11. Probability distribution of the contact stress σ^* for different yield strength as input to Persson's theory compared to GFDD for indentation using $\bar{h} = 0.01$ μm at $\sigma_0^* = 0.06$.

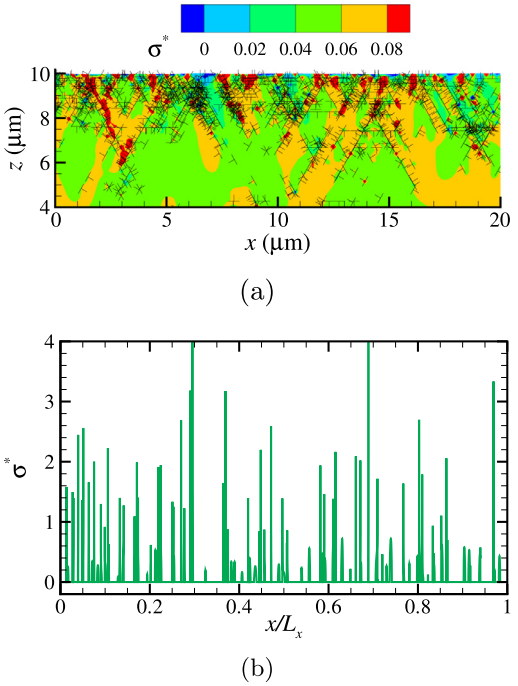

Fig. 12. (a) Dislocations, stress distribution and (b) contact tractions σ^* for an indenter with $\bar{h} = 0.01$ μm at an applied load $\sigma_0^* = 0.06$.

as the input yield strength σ_Y in Persson's theory, a much better agreement is found for the load–displacement curves. The yield strength is calculated at 0.2% offset strain, as indicated in Fig. 9b.

However, this type of fix is not sufficient to obtain agreement between the probability distributions of the contact stress, as one can see from Fig. 11, where the probability distribution is shown for the simulations and for Persson's theory with and without correction for σ_Y, for the indenter with $\bar{h} = 0.01$ μm. While the fix gives agreement between the areas that are not in contact, the simulations show a much higher probability of having smaller as well as larger contact stresses when compared to the theory. The contact and body stresses obtained through GFDD in a single simulation are shown in Fig. 12.

4.2. Effect of short-wavelength cut-off

In this section, we perform simulations for different roughness resolution by changing the small wavelength, while keeping the large wavelength constant. This corresponds to changing the fractal discretization ϵ_f. It is noteworthy that changing resolution does not correspond to scaling the contact problem. Changing resolution involves extending the range between small and large wavelength, i.e. adding smaller wavelengths to the surface, and therefore results in a different boundary value problem, with a different elastic and thus plastic response. Such simulations are therefore not suitable to highlight a plasticity size dependence. They might however give an indication on how appropriate it is to replace σ_Y in Persson's theory with $\sigma_Y(\lambda_s)$, as suggested in Persson (2006).

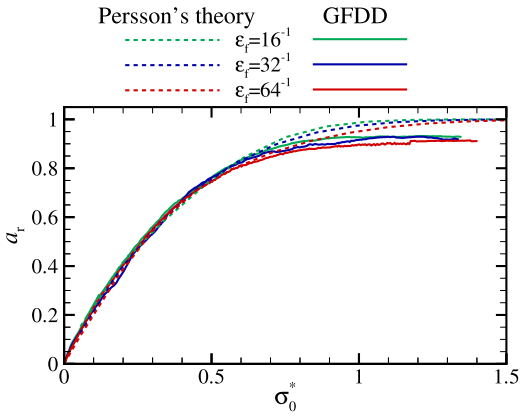

Fig. 13. Relative contact area a_r against reduced applied pressure σ_0^* for indenters with $\bar{h} = 0.001$ μm and three fractal discretizations ϵ_f.

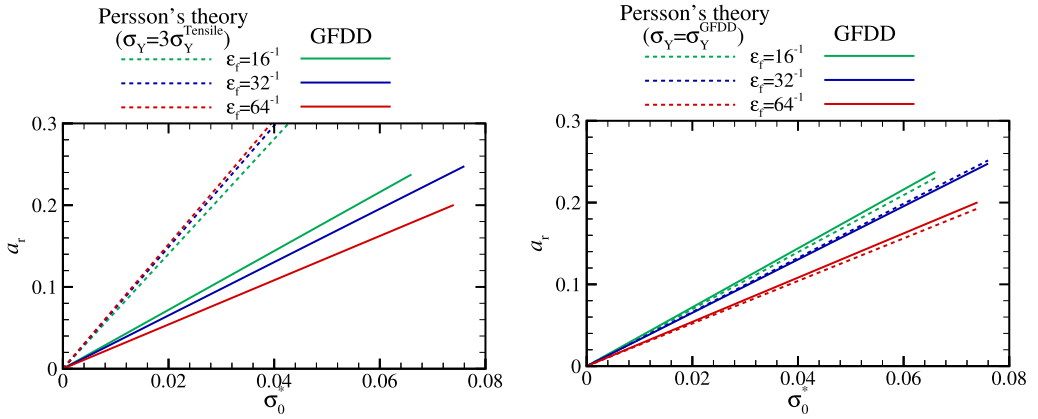

Fig. 14. Relative contact area a_r against reduced applied pressure σ_0^* for indenters with $\bar{h} = 0.01$ μm and three fractal discretizations ϵ_f. The input yield strength for Persson's theory is taken as (a) $\sigma_Y = 3\ \sigma_Y^{Tensile}$ (b) $\sigma_Y = \sigma_Y^{GFDD}$.

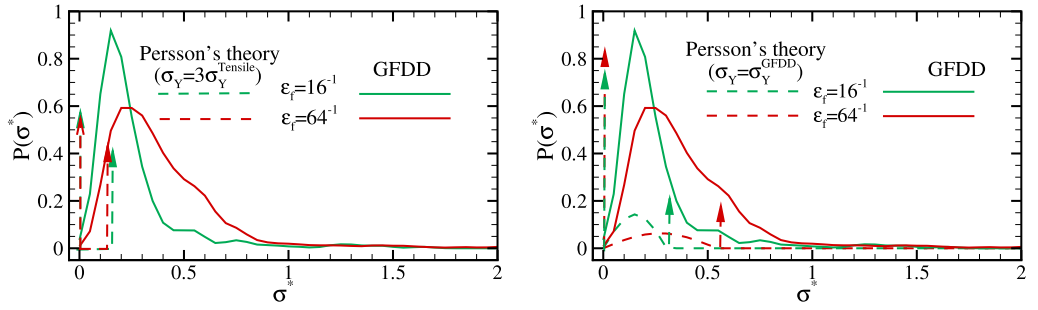

Fig. 15. Probability distribution of contact stress σ^* for different fractal discretizations ϵ_f for indentation for $\bar{h} = 0.01$ μm at $\sigma_0^* = 0.06$. The input yield strength for Persson's theory is taken as (a) $\sigma_Y = 3\ \sigma_Y^{Tensile}$ (b) $\sigma_Y = \sigma_Y^{GFDD}$.

Fig. 13 shows the increase of the relative contact area a_r with load for indenters with $\bar{h} = 0.001$ μm and three fractal discretizations. The curves are insensitive to a change in λ_s suggesting against the use of a resolution-dependent σ_Y. For all resolutions there is a good agreement between simulations and theory. If one instead considers indenters with $\bar{h} = 0.01$ μm the agreement is poor for all discretizations (see Fig. 14a). The agreement improves if again, instead of using $\sigma_Y = 3\sigma_Y^{Tensile}$ one uses $\sigma_Y = \sigma_Y^{GFDD}$ (see Fig. 14).

Given that σ_Y^{GFDD} is resolution-dependent, we conclude that indeed a $\sigma_Y(\lambda_s)$ should be used, as suggested in Persson (2006). However, the use of a resolution-dependent σ_Y is not sufficient to obtain the agreement between the probability distributions, as one can see in Fig. 15. Also, the dependence of σ_Y on resolution appears to be much more important than the dependence of σ_Y on rms height.

Table 3
Normalized yield strength $\sigma_Y^{GFDD}/3\sigma_Y^{Tensile}$.

rms height	$\epsilon_f = 4^{-1}$	$\epsilon_f = 8^{-1}$	$\epsilon_f = 16^{-1}$	$\epsilon_f = 32^{-1}$	$\epsilon_f = 64^{-1}$
$\bar{h} = 0.01$ μm	1.4	1.7	2.0	2.7	4.1
$\bar{h} = 0.1$ μm	3	4.7	9.5	10.6	13.3

Here in Table 3 we provide the flow stress σ_Y^{GFDD} found through GFDD simulations for indenters with $\bar{h} = 0.01$ μm and $\bar{h} = 0.1$ μm that allows for good agreement for area–load curves in Persson's theory. Data for $\bar{h} = 0.001$ μm are not reported, given that no correction is needed for agreement between area–load curves in that case.

5. Concluding remarks

In this paper, we have shown a comparison between dislocation dynamics simulations and Persson's theory in the study of contact between a flat metal body by a rigid indenter with self-affine roughness. Although there is a good agreement between simulations and theory when the metal behaves elastically, the agreement ceases to be good when there is plasticity. The best agreement for the area–load curves is found for small values of the rms height, when the response is close to elastic up to large contact fractions. This is because for small rms height, the onset of plasticity in dislocation dynamics simulations occurs at larger indentation depth than in a continuum theory, because there are only few discrete dislocation sources in the subsurface region where the stress concentration is sufficiently large to induce dislocation nucleation.

A good agreement between the area–load curves of simulations and theory is obtained also for larger rms heights if the size independent yield strength in the theory is replaced by the size-dependent yield strength obtained through the simulations.

The necessity of using a resolution-dependent yield strength in his plasticity theory was already explicitly mentioned by Persson. The fix is indeed important, because the plastic response depends on resolution. However, if one believes the results of the simulations (of course they have limitations too, to mention a couple of them: they are two dimensional and small strain), this fix is not sufficient. This is because it does not account for the plasticity size dependence that is observed when one or more geometrical length in the problem under study are scaled down: To account for this, the yield strength should become scale-dependent.

Another point that is important to consider is that, although we found good agreement for area–load curves, when using Persson's theory with the yield strength obtained through dislocation dynamics (i.e. a yield strength that depends on rms height and resolution) the contact stress probability distribution was still markedly different. The simulations predict a much broader contact stress distribution compared with the theory. This is because in the theory the material behaves as perfectly plastic, i.e., without any strain hardening. A possible improvement of the theory might be to use, instead of a constant yield strength, a yield strength that increases with plastic deformation. This would translate in a plastic peak in the probability distribution that moves towards larger pressures with increasing closure of the contact and a broader distribution in stresses of the elastic part of the contact.

Acknowledgement

This project has received funding from the European Research Council (ERC) under the European Union's Horizon 2020 research and innovation programme (grant agreement no. 681813).

References

Bouchaud, E., 1997. Scaling properties of cracks. J. Phys. 9, 4319. doi:10.1088/0953-8984/9/21/002.
Bouchaud, E., Lapasset, G., Planes, J., 1990. Fractal dimension of fractured surfaces: a universal value? EPL (Europhys. Lett.) 13, 73. doi:10.1209/0295-5075/13/1/013.
Bowden, F., Tabor, D., 2001. The friction and lubrication of solids. Clarendon Press. Number v. 1 in Oxford Classic Texts in the Physical Sciences.
Campañá, C., Müser, M.H., Robbins, M.O., 2008. Elastic contact between self-affine surfaces: comparison of numerical stress and contact correlation functions with analytic predictions. J. Phys. 20, 354013. doi:10.1088/0953-8984/20/35/354013.
Dapp, W., Prodanov, N., Müser, M., 2014. Systematic analysis of persson's contact mechanics theory of randomly rough elastic surfaces. J. Phys. Condens. Matter 26. doi:10.1088/0953-8984/26/35/355002.
Dauskardt, R., Haubensak, F., Ritchie, R., 1990. On the interpretation of the fractal character of fracture surfaces. Acta Metall. Mater. 38, 143–159. doi:10.1016/0956-7151(90)90043-G.
El-Awady, J.A., 2015. Unravelling the physics of size-dependent dislocation-mediated plasticity. Nat. Commun. 6, 5926. doi:10.1038/ncomms6926.
Fleck, N., Muller, G., Ashby, M., Hutchinson, J., 1994. Strain gradient plasticity: theory and experiment. Acta Metall. Mater. 42, 475–487. doi:10.1016/0956-7151(94)90502-9.
Van der Giessen, E., Needleman, A., 1995. Discrete dislocation plasticity: a simple planar model. Modell. Simul. Mater. Sci. Eng. 3, 689. doi:10.1088/0965-0393/3/5/008.
Greer, J.R., Oliver, W.C., Nix, W.D., 2005. Size dependence of mechanical properties of gold at the micron scale in the absence of strain gradients. Acta Mater. 53, 1821–1830. doi:10.1016/j.actamat.2004.12.031.
Gurtin, M.E., 2000. On the plasticity of single crystals: Free energy, microforces, plastic-strain gradients. J. Mech. Phys. Solids 48 (5), 989–1036. doi:10.1016/S0022-5096(99)00059-9.
Imre, A., Pajkossy, T., Nyikos, L., 1992. Electrochemical determination of the fractal dimension of fractured surfaces. Acta Metall. Mater. 40, 1819–1826. doi:10.1016/0956-7151(92)90168-E.

Johnson, K., 1987. Contact Mechanics. Cambridge University Press.
Kraft, O., Gruber, P.A., Monig, R., Weygand, D., 2010. Plasticity in confined dimensions. Rev. Mater. Res. 40, 293–317.
Krim, J., Palasantzas, G., 1995. Experimental observations of self-affine scaling and kinetic roughening at sub-micron lengthscales. Int. J. Modern Phys. B 09, 599–632. doi:10.1142/S0217979295000239.
Lechenault, F., Pallares, G., George, M., Rountree, C., Bouchaud, E., Ciccotti, M., 2010. Effects of finite probe size on self-affine roughness measurements. Phys. Rev. Lett. 104, 025502. doi:10.1103/PhysRevLett.104.025502.
Lorenz, B., Persson, B., 2009. Leak rate of seals: comparison of theory with experiment. EPL (Europhys. Lett.) 86, 44006. doi:10.1209/0295-5075/86/44006.
Lorenz, B., Persson, B.N.J., 2009. Interfacial separation between elastic solids with randomly rough surfaces: comparison of experiment with theory. J. Phys. 21, 015003. doi:10.1088/0953-8984/21/1/015003.
Ma, Q., Clarke, D.R., 1995. Size dependent hardness of silver single crystals. J. Mater. Res. 10, 853–863. doi:10.1557/JMR.1995.0853.
Majumdar, A., Tien, C., 1990. Fractal characterization and simulation of rough surfaces. Wear 136, 313–327. doi:10.1016/0043-1648(90)90154-3.
Mandelbrot, B.B., Passoja, D.E., Paullay, A.J., 1984. Fractal character of fracture surfaces of metals. Nature Publishing Group.
Manners, W., Greenwood, J., 2006. Some observations on Persson's diffusion theory of elastic contact. Wear 261, 600–610. doi:10.1016/j.wear.2006.01.007.
Nicola, L., der Giessen, E.V., Needleman, A., 2003. Discrete dislocation analysis of size effects in thin films. J. Appl. Phys. 93, 5920–5928. doi:10.1063/1.1566471.
Nix, W.D., Gao, H., 1998. Indentation size effects in crystalline materials: a law for strain gradient plasticity. J. Mech. Phys. Solids 46, 411–425. doi:10.1016/S0022-5096(97)00086-0.
Persson, B., 2006. Contact mechanics for randomly rough surfaces. Surface Sci. Rep. 61, 201–227. doi:10.1016/j.surfrep.2006.04.001.
Persson, B.N.J., 2001. Elastoplastic contact between randomly rough surfaces. Phys. Rev. Lett. 87, 116101. doi:10.1103/PhysRevLett.87.116101.
Persson, B.N.J., 2001. Theory of rubber friction and contact mechanics. J. Chem. Phys. 115, 3840–3861. doi:10.1063/1.1388626.
Plouraboué, F., Boehm, M., 1999. Multi-scale roughness transfer in cold metal rolling. Tribol. Int. 32, 45–57. doi:10.1016/S0301-679X(99)00013-4.
Venugopalan, S.P., Nicola, L., 2019. Indentation of a plastically deforming metal crystal with a self-affine rigid surface: a dislocation dynamics study. Acta Mater. 165, 709–721. doi:10.1016/j.actamat.2018.10.020.
Venugopalan, S.P., Müser, M.H., Nicola, L., 2017. Green's function molecular dynamics meets discrete dislocation plasticity. Modell. Simul. Mater. Sci. Eng. 25, 065018. doi:10.1088/1361-651x/aa7e0e.
Venugopalan, S.P., Nicola, L., Müser, M.H., 2017. Green's function molecular dynamics: including finite heights, shear, and body fields. Modell. Simul. Mater. Sci. Eng. 25, 034001. doi:10.1088/1361-651x/aa606b.
Volkert, C.A., Lilleodden, E.T., 2006. Size effects in the deformation of sub-micron au columns. Philos. Mag. 86, 5567–5579. doi:10.1080/14786430600567739.
Wang, A., Müser, M.H., 2017. Gauging Persson theory on adhesion. Tribol. Lett. 65, 103. doi:10.1007/s11249-017-0886-9.